Energy & Environmental Science

Accepted Manuscript

ROYAL SOCIETY OF CHEMISTRY

www.rsc.org/ees

Graphical abstract

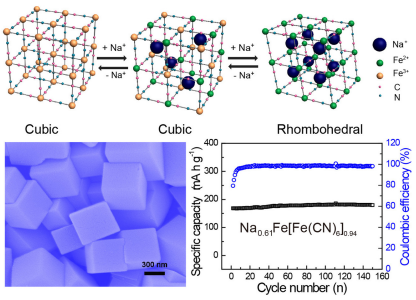

TOC text

High-quality Prussian blue crystals with low vacancy and water content show high specific capacity and remarkable cycle stability as cathode materials in Na-ion batteries.

Cite this: DOI: 10.1039/c0xx00000x

www.rsc.org/xxxxxx

ARTICLE TYPE

High-quality prussian blue crystals as superior cathode materials for room-temperature sodium-ion batteries

*Ya You, Xing-Long Wu, Ya-Xia Yin, and Yu-Guo Guo**

Received (in XXX, XXX) Xth XXXXXXXXX 20XX, Accepted Xth XXXXXXXXX 20XX

DOI: 10.1039/b000000x

High-quality Prussian blue crystals with low vacancies and water content are obtained by employing $Na_4Fe(CN)_6$ as the single iron-source precursor. The high-quality prussian blue shows high specific capacity and remarkable cycle stability as cathode material in Na-ion batteries because of its excellent ion storage capability and impressive structure stability during cycling.

Currently, the pursuit of rechargeable, advanced energy storage devices is critical for integrating renewable energy into smart electrical grids.[1, 2] Compared with Li-ion batteries, room-temperature Na-ion batteries are more suitable for large-scale applications, due to the more abundant reserves and lower price of Na.[3-13] Although numerous oxides and phosphate cathode materials have been demonstrated as good hosts for Na^+, development of feasible electrode materials with high capacity, long cycle life, and low cost remains a challenging issue that warrants further investigation.[14-25]

Prussian blue ($A_xFe[Fe(CN)_6]_y\cdot\square_{1-y}\cdot mH_2O$; A, alkaline metal; $\square$, $[Fe(CN)_6]$ vacancies occupied by coordinating water; $0 < x < 2$, $y < 1$; denoted as PB) and its analogues are considered as promising cathode materials for Na-ion batteries because of the following reasons: i) the rigid open framework with large interstitial sites can ensure acceptable Na^+ mobility and accommodate volume variation during Na^+ insertion/extraction;[26-31] ii) the theoretical specific capacity of PB is as high as 170 mA h g^{-1} [based on $Na_2FeFe(CN)_6$] because of a theoretical two-electron redox reaction;[32] iii) the facile synthetic procedure, nontoxicity and low cost of PB make it suitable for large-scale applications.[33-35] Nevertheless, the reported specific capacity of PB still falls far behind the theoretical value. Meanwhile, PB suffers from low Coulombic efficiency and poor cycling stability, which impedes its practical utilization. It is established that the electrochemical performance of PB is closely related to its intrinsic crystal structure.[36] The presence of $[Fe(CN)_6]$ vacancies occupied by coordinated water in PB are reported to be inefficient for Na^+ storage. In addition, $[Fe(CN)_6]$ vacancies may induce lattice distortion and even the Fe-C≡N-Fe bridge collapse during Na^+ insertion/extraction, further resulting in low specific capacity, low Coulombic efficiency, and electrochemical performance deterioration.[37] Unfortunately, PB prepared through the conventional synthetic method always exhibits large amounts of vacancies in the crystal framework because of rapid precipitation process.[38] Therefore, obtaining PB crystals with more perfect structures for room-temperature Na-ion batteries still remains challenging.

In this communication, we report the fabrication of high-quality PB nanocrystals $Na_{0.61}Fe[Fe(CN)_6]_{0.94}$ (HQ-NaFe) in the form of nanocubes through a facile synthetic procedure using $Na_4Fe(CN)_6$ as the only iron-source. Due to the slow growing process for crystal, HQ-NaFe exhibits low zeolite water and $[Fe(CN)_6]$ vacancies content in the crystal framework, which further results in an impressive ion-storage capability, sufficient transportation pathways for Na^+ and e^-, and effective maintenance of the crystal structure integrity upon cycling. Consequently, HQ-NaFe exhibits impressive electrochemical performance as cathode in Na-ion batteries in terms of high specific capacity (170 mA h g^{-1}) approaching its theoretical value, impressive cycling stability (no apparent capacity loss for even 150 cycles), excellent rate capability, and high Coulombic efficiency (~100%).

HQ-NaFe crystals were synthesized by single iron-source method, as illustrated in Fig. S1†. Typically, 100 mL $Na_4Fe(CN)_6$ and 1 mL hydrochloric acid (37%) solution are firstly maintained at 60 °C under vigorous stirring (Fig. S1a†). Under acidic environment, $[Fe(CN)_6]^{4-}$ is slowly decomposed to Fe^{2+} (Fig. S1b†). Fe^{2+} will subsequently be oxidized to Fe^{3+} due to its instability in the atmosphere (Fig. S1c†). Afterward, Fe^{2+}/Fe^{3+} reacts with the undecomposed $[Fe(CN)_6]^{4-}$ to form HQ-NaFe nanocube nuclei (Fig. S1d†). The sizes of HQ-NaFe cubes increase gradually with the reaction time (Fig. S1e and S2†). Finally, HQ-NaFe cubes with sizes of 300~600 nm are formed, as shown in the scanning electron microscopy (SEM) image in Fig. 1a. For comparison, low-quality PB nanoparticles (LQ-NaFe) are synthesized by directly mixing two solutions that contain $[Fe(CN)_6]^{4-}$ and Fe^{3+}, respectively. LQ-NaFe precipitates within a very short time and presents as granular morphology with size of ~20 nm (Fig. 1b). All the X-ray diffraction (XRD) peaks of both HQ-NaFe and LQ-NaFe can be well indexed to a pure face-centered-cubic phase (Fig. 1c), indicating that they exhibit the same crystal structure.[37] The calculated lattice parameters of HQ-NaFe and LQ-NaFe are 10.21 Å and 10.27 Å, respectively. Due to the rapid precipitation process, highly disordered $[Fe(CN)_6]$ vacancies are supposed to exist in LQ-NaFe, whereas the slower growing process for HQ-NaFe nanocubes is capable of producing a more perfect structure, which is further confirmed by the elemental content results obtained using elemental analyzer and inductively coupled plasma atomic emission spectroscopy (ICP-AES). According to the elemental contents of C, N, Na, and Fe

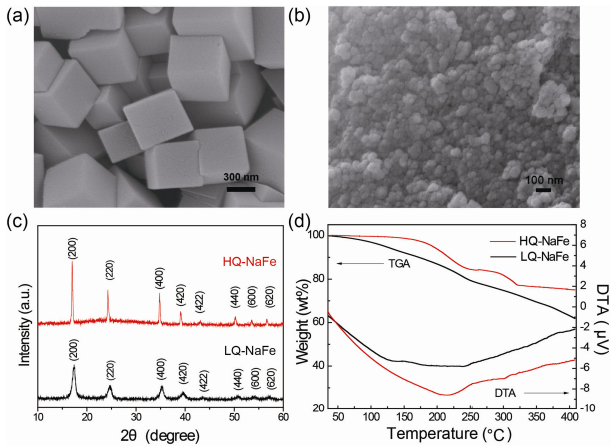

Fig. 1 Typical SEM images of (a) HQ-NaFe and (b) LQ-NaFe. (c) XRD patterns and (d) TG and DTA curves of the as-prepared HQ-NaFe and LQ-NaFe.

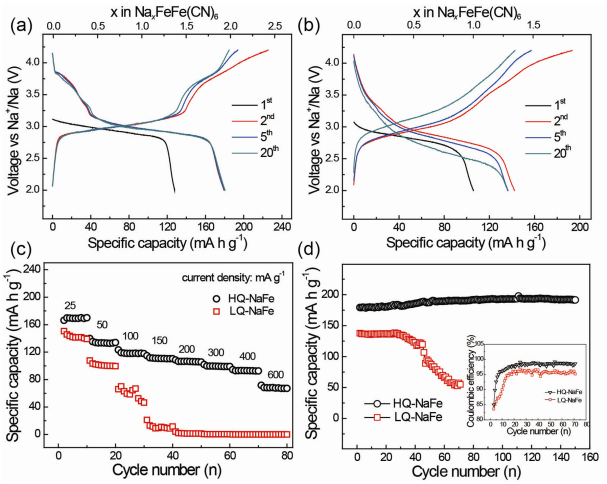

Fig. 2 Galvanostatic discharge/charge voltage profiles of (a) HQ-NaFe and (b) LQ-NaFe. (c) Rate capability of HQ-NaFe and LQ-NaFe. (d) Cycling performance of HQ-NaFe and LQ-NaFe under a current density of 25 mA g^{-1}. Inset is the Coulombic efficiencies of HQ-NaFe and LQ-NaFe.

for each product (Table S1), the as-prepared HQ-NaFe and LQ-NaFe are described by formulas $Na_{0.61}Fe[Fe(CN)_6]_{0.94}\bullet\square_{0.06}$ and $Na_{0.13}Fe[Fe(CN)_6]_{0.68}\bullet\square_{0.32}$, respectively. The formulas obtained above demonstrate that the $[Fe(CN)_6]$ vacancies content in HQ-NaFe is only 6%, which is much less than that in LQ-NaFe (32%). Besides, water molecules tend to accumulate at $[Fe(CN)_6]$ vacancies' sites, coordinated with Fe^{3+} octahedral to maintain the electroneutrality.[39] Therefore, the water content of HQ-NaFe is also reduced, which is proved by thermogravimetric (TG) and differential thermal analyses (DTA, Fig. 1d). The HQ-NaFe and LQ-NaFe water contents are 15.7 and 20.7 wt%, respectively. Meanwhile, the thermal stability of HQ-NaFe is significantly enhanced than that of LQ-NaFe, indicating a more stable structure for HQ-NaFe. Above all, through a facile single iron-source method, HQ-NaFe with less $[Fe(CN)_6]$ vacancies and crystal water content is obtained compared with LQ-NaFe synthesized by commonly used rapid precipitation synthetic process.

The performance of HQ-NaFe and LQ-NaFe as cathodes of room-temperature Na-ion batteries was tested by galvanostatic discharge and charge. The galvanostatic discharge and charge voltage profiles of HQ-NaFe and LQ-NaFe under a current density of 25 mA g^{-1} are shown in Fig. 2a and b, respectively. HQ-NaFe exhibits five reduction peaks between 4.0 and 2.7 V (*vs.* Na^+/Na) during discharge (Fig. S3a†). Given the muti-plateaus discharge profiles of HQ-NaFe, it can be speculated that Na^+ insertion undergoes a stepwise process, which is quite similar to the staging phenomenon in graphite.[40] In HQ-NaFe, Na^+ prefers to occupy some special sites in the framework to form a periodic array. However, only two broad cathodic peaks are observed at 3.4 and 2.7 V for LQ-NaFe (Fig. S3b†), indicating a quite different Na^+ diffusion process. The difference between Na^+ insertion/extraction behaviors for HQ-NaFe and LQ-NaFe may be caused by the nanometer size effects of LQ-NaFe. The specific mechanism is still under investigation. The discharge capacity of HQ-NaFe is as high as its theoretical capacity (170 mA h g^{-1}), which corresponds to a full utilization of HQ-NaFe material with two Na^+ insertion per molecule. The discharging capacity is much lower for LQ-NaFe (140 mA h g^{-1}, 1.3 Na^+ per molecule) because $[Fe(CN)_6]$ vacancies have been convinced to decrease the ion storage ability of PB.[36] The results indicate that the HQ-NaFe with low $[Fe(CN)_6]$ vacancies shows high specific capacity.

In addition, polarization between the charge and discharge voltage plateaus for HQ-NaFe is much lower (ca. 60 mV) compared with those for LQ-NaFe (ca. 200 mV, Fig. S4†). Voltage polarization is closely related to the e^- and Na^+ transportation among electrodes.[41] The $[Fe(CN)_6]$ vacancies in the PB crystal lattice may hinder the transportation of e^- along the C≡N framework. Furthermore, crystal water molecules compete with Na^+ to occupy the interstitial sites and inhibit Na^+ diffusion. Thus, LQ-NaFe exhibits a more sluggish kinetics, which will be discussed later. As a result, HQ-NaFe also exhibits higher specific capacities, especially under high discharge and charge currents, compared with those of LQ-NaFe (Fig. 2c). Under high current densities (> 150 mA g^{-1}), the specific capacities of LQ-NaFe decrease rapidly and approach zero value finally. However, the specific capacities of HQ-NaFe could be maintained at 110 and 70 mA h g^{-1} under 150 and 600 mA g^{-1}, respectively. The HQ-NaFe crystals with fewer vacancies are primarily capable of ensuring effective transportation pathways for both e^- and Na^+, which leads to a much more decreased polarization and improved rate capability than LQ-NaFe.

To further understand the kinetics of electrode reaction, electrochemical impedance spectroscopy (EIS) are investigated as shown in Fig. S5†. The Nyquist plots for HQ-NaFe and LQ-NaFe electrodes are composed of a depressed semicircle in the high-frequency region and a sloping line in the low-frequency region, which can be assigned to the charge-transfer process and the semi-infinite Warburg diffusion process, respectively (Fig. S5a†). The charge-transfer resistance of HQ-NaFe electrode (867 Ω) is much less than that of LQ-NaFe (3308 Ω), indicating a higher electronic conductivity and faster electrochemical reaction of HQ-NaFe electrode. The apparent diffusion coefficient *D* of Na^+ is calculated from the inclined line in the Warburg region (Fig. S5b†). The *D* value of HQ-NaFe and LQ-NaFe are 1.81×10^{-13}

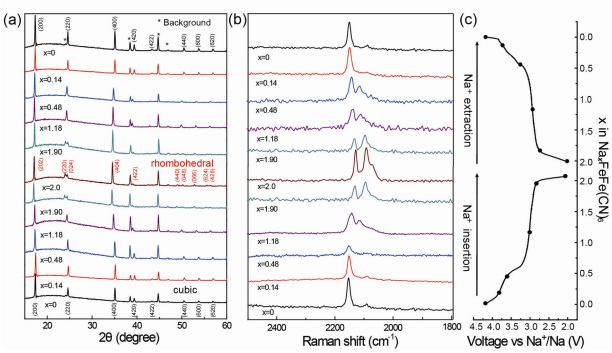

Fig. 3 (a) *Ex situ* XRD patterns of HQ-NaFe electrodes at various discharge and charge states. Black indexes correspond to the cubic phase, while red indexes correspond to the rhombohedral phase. (b) *Ex situ* Raman spectra of HQ-NaFe electrodes at various discharge and charge states. (c) Typical discharge/charge profiles of HQ-NaFe electrodes.

$cm^2\ s^{-1}$ and $8.13 \times 10^{-14}\ cm^2\ s^{-1}$, respectively. Therefore, HQ-NaFe with less water/vacancies content not only exhibits a faster electrochemical reaction, but also shows a higher ability for Na^+ diffusion, further demonstrating its faster kinetics.

Furthermore, HQ-NaFe exhibits significantly improved cycling performance than LQ-NaFe. For HQ-NaFe, the shape and voltage plateaus are well maintained for 150 cycles, without any increase of voltage polarization. The discharge capacity of HQ-NaFe remains as high as 170 mA h g^{-1} without apparent capacity loss for 150 cycles (Fig. 2d). However, the capacity of LQ-NaFe decreases rapidly with only 36.5% capacity retention after 70 cycles. Meanwhile, the Coulombic efficiency of HQ-NaFe (98%) is higher than that of LQ-NaFe (95%, inset in Fig. 2d). The improved Coulombic efficiency for HQ-NaFe is mainly attributed to the reduced water content inside the crystal framework.[42] Zeolite water decomposition during the charging process will lead to low Coulombic efficiency in the first cycle and deteriorate the battery performance during the following cycle. The large surface area of nanosized LQ-NaFe can cause unfavorable side effects, resulting in decreased Coulombic efficiency as well. The premise that zeolite water could be removed completely is questionable, and minimizing PB water content still requires further study.

It has been convinced that PB shows a tendency to degrade upon exposure to light, thereby inhibiting its practical applications.[43] We compared the electrochemical performances of HQ-NaFe and LQ-NaFe stored in ambient condition for 4 months. Surprisingly, HQ-NaFe still shows good electrochemical performance with a capacity of 130 mA h g^{-1}, whereas LQ-NaFe loses its electrochemical activity completely (Fig. S6†). The findings indicate that the structural stability of PB under light irradiation can be drastically enhanced by improving the quality of the crystal structure. The above results also prove that developing PB with high-quality crystal structures would lead to advancements in its applications in industrial production.

The electrochemical reaction mechanism of HQ-NaFe was investigated through *ex situ* XRD and Raman tests. *Ex situ* XRD patterns of the electrodes at different discharge/charge states are shown in Fig. 3a. During Na^+ insertion process, the positions of

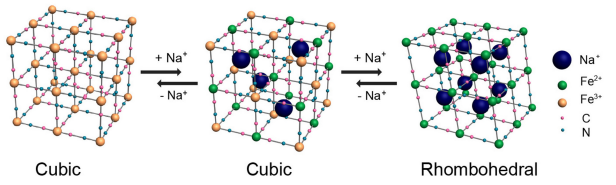

Fig. 4 Schemetic illustration of the redox mechanism of HQ-NaFe.

XRD peaks shift gradually toward smaller angle (increase of the lattice parameter) and the crystal structure of HQ-NaFe changes from cubic to rhombohedral when x in $Na_xFeFe(CN)_6$ is as high as 2.0,[44] demonstrating that high Na concentration reduces crystal symmetry. The structure change is highly reversible during Na^+ extraction process. *Ex situ* Raman was employed to illustrate the valance state change of iron during cycling because the frequency of the cyanide vibration stretching mode, ν (CN), is sensitive to the oxidation state of the coordinating iron (Fig. 3b). During the insertion of Na^+, ν (CN) bands shift gradually toward low wave number positions and changed from 2153, 2129 and 2096 cm^{-1} (x = 0) to 2129, 2096, and 2073 cm^{-1} (x = 2.0), indicating that Fe^{3+} is reduced to Fe^{2+}, and *vice versa*.[43] The schematic illustration of HQ-NaFe redox mechanism is shown in Fig. 4. HQ-NaFe undergoes a two-electron redox reaction: cubic $Fe^{III}Fe^{III}(CN)_6$ ↔ cubic $NaFe^{III}Fe^{II}(CN)_6$ ↔ rhombohedral $Na_2Fe^{II}Fe^{II}(CN)_6$. This redox reaction is favored because the perfect structure of HQ-NaFe with high stability promotes its ability to accommodate large mechanical strain and volume variation during two Na-ions insertion/extraction and prevents the collapse of the crystal framework. The morphology and structure of HQ-NaFe can be well preserved even after 150 cycles (Fig. S7 and S8†). Both XRD and Raman results show that the electrochemical reaction of HQ-NaFe is highly reversible, which also contributes to its impressive cycling stability.

Conclusions

In summary, high-quality PB crystals with low crystal water and $[Fe(CN)_6]$ vacancies content are obtained using a facile synthetic method. It's found that water and vacancies have significant effects on their electrochemical performances as cathode materials in Na-ion batteries. On one hand, the $[Fe(CN)_6]$ vacancies can decrease the electronic conductivity of PB and lead to framework collapse and disordered lattice during cycling. On the other hand, the occupancy of interstitial sites by water molecules inhibits Na^+ insertion and transport, and the decomposition of water deteriorates the Coulombic efficiency and cycling performance. As a result, HQ-NaFe with less vacancies and water content exhibits high specific capacity of 170 mA h g^{-1} by realizing a two-electron reaction, an impressive cycling stability without apparent capacity loss for 150 cycles, and a high Coulombic efficiency of ~100%, making HQ-NaFe a promising candidate for long lifespan Na-ion batteries. In addition, HQ-NaFe shows much decreased charge-transfer resistance and higher Na^+ diffusion coefficient than LQ-NaFe, further proving that the presence of water/vacancies will deteriorate the electronic conductivity and inhibit the diffusion of Na^+. HQ-NaFe undergoes a two-electron redox reaction: cubic

$Fe^{III}Fe^{III}(CN)_6$ ↔ cubic $NaFe^{III}Fe^{II}(CN)_6$ ↔ rhombohedral $Na_2Fe^{II}Fe^{II}(CN)_6$. The use of high-quality PB crystals might put new insight for the design of high-performance and high-stability cathode materials of room-temperature Na-ion batteries.

Acknowledgements

This work was supported by the National Natural Science Foundation of China (Grant Nos. 51225204, 91127044 and 21121063), the National Key Project on Basic Research (Grant Nos. 2012CB932900 and 2011CB935700).

Notes and references

CAS Key Laboratory of Molecular Nanostructure and Nanotechnology, and Beijing National Laboratory for Molecular Sciences, Institute of Chemistry, Chinese Academy of Sciences (CAS), Beijing 100190, P.R. China. E-mail: ygguo@iccas.ac.cn; Fax & Tel: +86-10-82617069

† Electronic Supplementary Information (ESI) available: Experimental section, additional data on HQ-NaFe and LQ-NaFe. See DOI: 10.1039/b000000x/

1 B. Dunn, H. Kamath and J.-M. Tarascon, *Science.*, 2011, **334**, 928-935.
2 X. N. Xie, Y. Wang, Q. Wang and K. P. Loh, *Adv. Mater.*, 2012, **24**, 76-81.
3 V. Palomares, M. Casas-Cabanas, E. Castillo-Martinez, M. H. Han and T. Rojo, *Energy Environ. Sci.*, 2013, **6**, 2312-2337.
4 M. D. Slater, D. Kim, E. Lee and C. S. Johnson, *Adv. Funct. Mater.*, 2013, **23**, 947-958.
5 J. Jiang, Y. Li, J. Liu, X. Huang, C. Yuan and X. W. Lou, *Adv. Mater.*, 2012, **24**, 5166-5180.
6 H.-X. Ji, X.-L. Wu, L.-Z. Fan, C. Krien, I. Fiering, Y.-G. Guo, Y. Mei and O. G. Schmidt, *Adv. Mater.*, 2010, **22**, 4591-4595.
7 P. Han, Y. Yue, L. Zhang, H. Xu, Z. Liu, K. Zhang, C. Zhang, S. Dong, W. Ma and G. Cui, *Carbon*, 2012, **50**, 1355-1362.
8 Y. Yao, N. Liu, M. T. McDowell, M. Pasta and Y. Cui, *Energy Environ. Sci.*, 2012, **5**, 7927-7930.
9 V. Palomares, P. Serras, I. Villaluenga, K. B. Hueso, J. Carretero-Gonzalez and T. Rojo, *Energy Environ. Sci.*, 2012, **5**, 5884-5901.
10 J.-Y. Luo, W.-J. Cui, P. He and Y.-Y. Xia, *Nat. Chem.*, 2010, **2**, 760-765.
11 L. Yang, S. Wang, J. Mao, J. Deng, Q. Gao, Y. Tang and O. G. Schmidt, *Adv. Mater.*, 2013, **25**, 1180-1184.
12 S. Y. Hong, Y. Kim, Y. Park, A. Choi, N.-S. Choi and K. T. Lee, *Energy Environ. Sci.*, 2013, **6**, 2067-2081.
13 H. Pan, Y.-S. Hu and L. Chen, *Energy Environ. Sci.*, 2013, **6**, 2338-2360.
14 Z. Jian, W. Han, X. Lu, H. Yang, Y.-S. Hu, J. Zhou, Z. Zhou, J. Li, W. Chen, D. Chen and L. Chen, *Adv. Energy Mater.*, 2013, **3**, 156-160.
15 R. Berthelot, D. Carlier and C. Delmas, *Nat. Mater.*, 2011, **10**, 74-80.
16 N. Yabuuchi, M. Kajiyama, J. Iwatate, H. Nishikawa, S. Hitomi, R. Okuyama, R. Usui, Y. Yamada and S. Komaba, *Nat. Mater.*, 2012, **11**, 512-517.
17 Y.-U. Park, D.-H. Seo, H.-S. Kwon, B. Kim, J. Kim, H. Kim, I. Kim, H.-I. Yoo and K. Kang, *J. Am. Chem. Soc.*, 2013, **135**, 13870-13878.
18 H. Zhu, Z. Jia, Y. Chen, N. Weadock, J. Wan, O. Vaaland, X. Han, T. Li and L. Hu, *Nano Lett.*, 2013, **13**, 3093-3100.
19 K. Tang, L. Fu, R. J. White, L. Yu, M.-M. Titirici, M. Antonietti and J. Maier, *Adv. Energy Mater.*, 2012, **2**, 873-877.
20 M. Dollé, S. Patoux and M. M. Doeff, *Chem. Mater.*, 2005, **17**, 1036-1043.
21 D. A. Stevens and J. R. Dahn, *J. Electrochem. Soc.*, 2000, **147**, 1271-1273.
22 H.-G. Wang, Z. Wu, F.-L. Meng, D.-L. Ma, X.-L. Huang, L.-M. Wang and X.-B. Zhang, *ChemSusChem*, 2013, **6**, 56-60.
23 A. Ponrouch, R. Dedryvere, D. Monti, A. E. Demet, J. M. Ateba Mba, L. Croguennec, C. Masquelier, P. Johansson and M. R. Palacin, *Energy Environ. Sci.*, 2013, **6**, 2361-2369.
24 Q. Qu, L. Fu, X. Zhan, D. Samuelis, J. Maier, L. Li, S. Tian, Z. Li and Y. Wu, *Energy Environ. Sci.*, 2011, **4**, 3985-3990.
25 Y. Wang, P. He and H. Zhou, *Energy Environ. Sci.*, 2011, **4**, 4994-4999.
26 T. Matsuda, M. Takachi and Y. Moritomo, *Chem. Commun.*, 2013, **49**, 2750-2752.
27 L. Wang, Y. Lu, J. Liu, M. Xu, J. Cheng, D. Zhang and J. B. Goodenough, *Angew. Chem. Int. Ed.*, 2013, **52**, 1964-1967.
28 M. Zhou, J. Qian, X. Ai and H. Yang, *Adv. Mater.*, 2011, **23**, 4913-4917.
29 H. Lee, Y.-I. Kim, J.-K. Park and J. W. Choi, *Chem. Commun.*, 2012, **48**, 8416-8418.
30 C. D. Wessells, S. V. Peddada, R. A. Huggins and Y. Cui, *Nano Lett.*, 2011, **11**, 5421-5425.
31 C. D. Wessells, R. A. Huggins and Y. Cui, *Nat. Commun.*, 2011, **2**, 550-554.
32 M. Okubo, D. Asakura, Y. Mizuno, J. D. Kim, T. Mizokawa, T. Kudo and I. Honma, *J. Phys. Chem. L*, 2010, **1**, 2063-2071.
33 M. Pasta, C. D. Wessells, R. A. Huggins and Y. Cui, *Nat. Commun.*, 2012, **3**, 1149.
34 Y. Mizuno, M. Okubo, K. Kagesawa, D. Asakura, T. Kudo, H. Zhou, K. Oh-ishi, A. Okazawa and N. Kojima, *Inorg. Chem.*, 2012, **51**, 10311-10316.
35 Y. Mizuno, M. Okubo, E. Hosono, T. Kudo, H. Zhou and K. Oh-ishi, *J. Phys. Chem. C*, 2013, **117**, 10877-10882.
36 D. Asakura, M. Okubo, Y. Mizuno, T. Kudo, H. Zhou, K. Ikedo, T. Mizokawa, A. Okazawa and N. Kojima, *J. Phys. Chem. C*, 2012, **116**, 8364-8369.
37 X. Wu, W. Deng, J. Qian, Y. Cao, X. Ai and H. Yang, *J. Mater. Chem. A*, 2013, **1**, 10130-10134.
38 D. Asakura, C. H. Li, Y. Mizuno, M. Okubo, H. Zhou and D. R. Talham, *J. Am. Chem. Soc.*, 2013, **135**, 2793-2799.
39 P. R. Bueno, D. Gimenez-Romero, C. Gabrielli, J. J. Garcia-Jareno, H. Perrot and F. Vicente, *J. Am. Chem. Soc.*, 2006, **128**, 17146-17152.
40 S. M. Haight, D. T. Schwartz and M. A. Lilga, *J. Electrochem. Soc.*, 1999, **146**, 1866-1872.
41 X.-L. Wu, L.-Y. Jiang, F.-F. Cao, Y.-G. Guo and L.-J. Wan, *Adv. Mater.*, 2009, **21**, 2710-2714.
42 Y. Lu, L. Wang, J. Cheng and J. B. Goodenough, *Chem. Commun.*, 2012, **48**, 6544-6546.
43 L. Samain, B. Gilbert, F. Grandjean, G. J. Long and D. Strivay, *J. Anal. At. Spectrom.*, 2013, **28**, 524-535.
44 T. Matsuda, J. Kim and Y. Moritomo, *J. Am. Chem. Soc.*, 2010, **132**, 12206-12207.

Broader context

Currently, the pursuit of rechargeable advanced energy storage devices is critical for smoothly integrating renewable energy such as wind, solar, and tide into the smart electrical grid. Among the potential energy storage technologies, sodium-ion batteries are emerging as an appealing choice, especially for large-scale stationary energy storage, because Na is a worldwide abundance material with low cost. Prussian blue (PB) shows promising applications as cathode materials in Na-ion batteries because the facile synthetic procedure, nontoxicity themselves as well as low-cost. However, PB prepared by the conventional synthetic method always suffers from low Coulombic efficiency and poor cycling stability, which may be attributed to the imperfect and unstable crystal structure with large amounts of $[Fe(CN)_6]$ vacancies and coordinated water in the crystal framework. In the present work, we developed a facile synthetic procedure using $Na_4Fe(CN)_6$ as the only iron-source to fabricate high-quality PB crystals with low crystal water and $[Fe(CN)_6]$ vacancies content. These PB crystals show high specific capacity, impressive cycling stability and Coulombic efficiency. The use of high-quality PB crystals might open new insights into the design of high-performance and high-stability cathode materials of room-temperature Na-ion batteries.